

EFFECTS OF HETEROGENEOUS LITHOLOGY AND FOCUSED FLUID FLOW ON GAS HYDRATE DISTRIBUTION IN MARINE SEDIMENTS

Sayantana Chatterjee, Guangsheng Gu, Walter G. Chapman, George J. Hirasaki*
Department of Chemical and Biomolecular Engineering, Rice University
Houston, Texas, 77005
United States of America

Gaurav Bhatnagar
Shell International Exploration and Production Inc.
Houston, Texas, 77082
United States of America

Brandon Dugan, Gerald R. Dickens
Department of Earth Science, Rice University
Houston, Texas, 77005
United States of America

ABSTRACT

We simulate gas hydrate and free gas accumulation in heterogeneous marine sediments over geologic time scales. Simulations with a vertical fracture network, which extends through the gas hydrate stability zone and has permeability 100 times greater than the surrounding shale formation, show that focused fluid flow causes higher hydrate (25-55%) and free gas saturation (30-45%) within the fracture network compared to the surrounding, lower permeability shale. Systems with high permeability, dipping sand layers also show localized, elevated saturations of hydrate (60%) and free gas (40%) within the sand layers due to focused fluid flow. Permeability anisotropy, with a vertical to horizontal permeability ratio on the order of 10^{-2} , enhances hydrate concentrations within high permeability conduits because anisotropy enhances transport of methane-charged fluid to high permeability conduits. Our two-dimensional (2-D), heterogeneous models quantify how focused fluid flow through high permeability zones affects local hydrate accumulation and saturation. We also show increased fluid flux and deep source methane input result in enhanced concentrations of hydrate and free gas, and also increase the flow focusing effects. From our 2-D results, we determine that the hydrate and free gas saturations can be characterized by the local Peclet number (localized, focused, advective flux relative to diffusion); which is consistent with Peclet number characterization in one-dimensional (1-D) systems. This characterization suggests that even in lithologically complex systems, local hydrate and free gas saturations can be characterized by basic parameters (local flux and diffusivity).

Keywords: Gas hydrate, focused fluid flow, heterogeneity, local fluid flux, numerical modeling

NOMENCLATURE

c_i^j	Mass fraction of component i in phase j	g	Acceleration due to gravity
$c_{m,eqb}^l$	CH ₄ solubility at the base of the GHSZ	k	Absolute sediment permeability tensor
Da	Damköhler number	k_o	Absolute sediment permeability at seafloor
D_m	Diffusivity of CH ₄ in seawater	k_{rj}	Relative permeability of phase j

k_{rj}^o	End-point value of k_{rj}
L_o	Depth of the seafloor ($\tilde{z} = 0$)
L_t	Depth to the base of the GHSZ
L_z	Depth to the base of the domain
L_x	Width of the domain
L_c	Characteristic depth of compaction
M_i	Molecular weight of component i
N_{SC}	Sedimentation-compaction group
N'_{tv}	Porosity and compaction group
n	Pore size distribution index
Pe_1	First Peclet number
Pe_2	Second Peclet number
p_j	Pressure of phase j
P_c	Capillary pressure
$P_{c,o}$	Capillary pressure at reference value
$P_{ce,o}$	Capillary entry pressure at reference value
S_j	Saturation of phase j
S_{jr}	Residual saturation of phase j
\dot{S}	Sedimentation rate
t	Time
$U_{f, sed}$	Fluid flux due to sedimentation
$U_{f, ext}$	Fluid flux due to external fluid flow
v_j	Velocity of phase j
z	Depth below the seafloor
α	Organic carbon content in sediment
α_o	Organic carbon content at the seafloor
β	Normalized carbon content at the seafloor
η, γ	Reduced porosity parameters
λ	Kinetic rate constant for methanogenesis
μ_j	Viscosity of phase j
ρ_j	Density of phase j
σ_v	Vertical effective stress
σ_c	Characteristic stress of compaction
σ_{gw}	Interfacial tension at gas-water contact
θ	Gas-water contact angle
ϕ	Porosity
ϕ_o	Porosity at the seafloor
ϕ_∞	Porosity at infinite depth

Subscripts/Superscripts:

g, h	Gas and hydrate phase
l, s	Liquid and sediment phase
m	CH ₄ component
w	Water component

INTRODUCTION

Solid gas hydrates can form when low molecular weight gas molecules and water combine at relatively high gas concentrations, high pressures, low temperatures, and low salinity conditions [1]. These conditions are present along many

continental margins (as well as in permafrost environments) where hydrocarbon gases, especially CH₄, accumulate in sediment pore space within a finite depth interval known as the gas hydrate stability zone (GHSZ). While the amount and distribution of marine gas hydrates remain uncertain [2,3], they may constitute a potential energy source [4,5], a deep-water geohazard [6,7], and an important component of the global carbon cycle [8,9]. Numerous studies have shown that gas hydrate and free gas accumulation in marine sediments is highly heterogeneous at the m-scale [e.g., 10, 11,12], which complicates views on their formation. To address this issue, we develop a 2-D, heterogeneous sedimentation-fluid flow model that tracks gas hydrate accumulation over geologic time scales.

BACKGROUND

Previous numerical models have coupled mass, momentum and energy transport equations to obtain steady-state solutions for gas hydrate distribution in marine sediments [e.g., 13,14,15]. In particular, *Davie and Buffett* [15] proposed a 1-D numerical model for hydrate accumulation due to biogenic sources of methane. This type of modeling has now been extended for specific sites. *Bhatnagar and co-workers* developed a generalized 1-D numerical model for gas hydrate accumulation and distribution in marine sediments over geologic time scales. This 1-D model could explain first-order observations at many sites and provide insights into gas hydrate systems behavior [16]. Through component balances, thermodynamic equilibrium, and key dimensionless groups, they established a correlation between the net fluid flux and the average hydrate saturation [16].

These types of homogeneous 1-D models provide first-order insights on hydrate occurrence, but do not capture the complexity and heterogeneity observed in natural gas hydrate systems. Fracture network systems and dipping permeable layers are common heterogeneities in natural gas hydrate settings; these localize flow, resulting in accumulation of localized, concentrated hydrate deposits [12]. To incorporate these heterogeneous features, lateral fluid flow and to broaden our knowledge of primary controls of hydrate concentration and distribution, we extend to two dimensions.

Heterogeneities we include are fracture networks and high permeability sand layers. We formulate the 2-D model through component mass balances and present some key results to show how lithologic heterogeneity causes regions of focused fluid flux. Higher saturations of hydrate and free gas are observed in these higher permeability regions as a result of the increased, localized, focused fluid flux. We simulate conditions for generalized parameters but our generalized model can be applicable to many heterogeneous sites.

MATHEMATICAL MODEL

General framework

Our 2-D model incorporates deposition and compaction of sediment, *in situ* methane generation, and migration of water with dissolved gas.

Component mass balances

The mass balances for water, sediment, organic carbon and methane are [17]:

Water:

$$\begin{aligned} & \frac{\partial}{\partial t} [\phi S_w c_w^l \rho_w + \phi S_h c_w^h \rho_h] \\ & + \nabla \cdot [\phi S_w c_w^l \rho_w v_w + \phi S_h c_w^h \rho_h v_h] = 0 \end{aligned} \quad (1)$$

Sediment:

$$\frac{\partial}{\partial t} [(1-\phi)\rho_s] + \nabla \cdot [(1-\phi)\rho_s v_s] = 0 \quad (2)$$

Organic material:

$$\begin{aligned} & \frac{\partial}{\partial t} [(1-\phi)\rho_s \alpha] + \nabla \cdot [(1-\phi)\rho_s v_s \alpha] \\ & = -\rho_s \lambda (1-\phi) \alpha \end{aligned} \quad (3)$$

Methane:

$$\begin{aligned} & \frac{\partial}{\partial t} [\phi S_w c_m^l \rho_w + \phi S_h c_m^h \rho_h + \phi S_g c_m^g \rho_g] \\ & + \nabla \cdot [\phi S_w c_m^l \rho_w v_w + \phi S_h c_m^h \rho_h v_s + \phi S_g c_m^g \rho_g v_g] \end{aligned}$$

$$= \nabla \cdot [\phi S_w \rho_w D_m \nabla \cdot c_m^l] + \frac{M_{CH_4}}{M_{org}} \rho_s \lambda (1-\phi) \alpha \quad (4)$$

Constitutive relationships

Water flux in a compacting medium is given by Darcy's law [18]:

$$S_w \phi (v_w - v_s) = -\frac{k k_{rw}}{\mu_w} \cdot (\nabla p_w - \rho_w g \nabla z) \quad (5)$$

Darcy's law for flux of free gas is [18]:

$$S_g \phi (v_g - v_s) = -\frac{k k_{rg}}{\mu_g} \cdot (\nabla p_g - \rho_g g \nabla z) \quad (6)$$

Absolute sediment permeability is defined as a power law function of porosity [19]:

$$k = k_o (\phi/\phi_o)^8 \quad (7)$$

Reduction in absolute sediment permeability due to formation of gas hydrates as a pore-filling structure is modeled by [20]:

$$k(\phi, S_h) = k_o(\phi) \left(1 - S_h^2 + \frac{2(1-S_h)^2}{\ln(S_h)} \right) \quad (8)$$

Relative permeability of water in the presence of free gas is modeled as [18]:

$$k_{rw} = k_{rw}^o (S_w^*)^4 \quad \text{where } S_w^* = \frac{S_w - S_{wr}}{1 - S_{wr}} \quad (9)$$

Gas relative permeability in the presence of water is given as [18]:

$$k_{rg} = k_{rg}^o (S_g^*)^2 \quad \text{where } S_g^* = \frac{S_g - S_{gr}}{1 - S_{wr} - S_{gr}} \quad (10)$$

The water, hydrate and gas phase saturations must equal unity:

$$S_w + S_h + S_g = 1 \quad (11)$$

Capillary pressure is defined as the difference between gas and pore water pressure:

$$P_c = p_g - p_w \quad (12)$$

The Leverett J-function $J(S_w)$ is used to normalize capillary pressure profiles as:

$$J(S_w) = \frac{P_{c,0}(S_w)}{\sigma_{gw} \cos \theta} \sqrt{\frac{k_o}{\phi_o}} \quad (13)$$

Assuming σ_{gw} and θ as constants, capillary pressure for any ϕ and k is:

$$P_c(S_w) = J(S_w) \sigma_{gw} \cos \theta \sqrt{\frac{\phi}{k}} = P_{c,0}(S_w) \sqrt{\frac{k_o \phi}{k \phi_o}} \quad (14)$$

The reference capillary pressure curve is defined by the Brooks-Corey model [18]:

$$P_{c,0}(S_w) = P_{ce,0} (S_w^*)^{-1/n} \quad (15)$$

We assume porosity is controlled by effective stress [21]:

$$\phi = \phi_\infty + (\phi_0 - \phi_\infty) e^{-\frac{\sigma_v - p_w}{\sigma_\phi}} \quad (16)$$

Lithostatic stress gradient is defined as a function of porosity and densities as:

$$\frac{\partial \sigma_v}{\partial z} = [(1 - \phi) \rho_s + \phi \rho_w] g \quad (17)$$

Scaled variables and key dimensionless groups

The above equations are normalized [e.g., 16, 17]. Reduced porosities are:

$$\tilde{\phi} = \frac{\phi - \phi_\infty}{1 - \phi_\infty} \quad \eta = \frac{\phi_0 - \phi_\infty}{1 - \phi_\infty} \quad \gamma = \frac{1 - \phi_\infty}{\phi_\infty} \quad (18)$$

Sedimentation and compaction in our model is assumed to be 1-D with zero lateral strain. This enables the sediment to move and deform vertically, but not laterally. Sediment is deposited on the seafloor and moves down with a z-component of velocity (v_s). Any gas hydrate within the formation and immobile free gas below critical saturation move with the same sediment velocity.

Above the critical saturation, the free gas is mobile, and free to migrate upwards and laterally.

Marine gas hydrate systems are often characterized by overpressure; i.e. pore water pressure is greater than hydrostatic. However, due to the presence of high permeability zones, which provide low resistance to flow, fluids focus within high permeability conduits. Natural systems are also anisotropic, with the ratio of vertical to horizontal permeability (k_v/k_h) less than unity. In such systems, greater horizontal permeability would focus more fluids from neighboring regions to the high permeability conduits by lateral migration.

The sedimentation rate at the seafloor can be defined as:

$$\dot{S} = v_s \text{ at } \tilde{z} = 0 \quad (19)$$

The sediment flux is given by:

$$U_s = \dot{S}(1 - \phi_o) \quad (20)$$

Peclet numbers are defined by the ratio of advective fluid flux to methane diffusion. Peclet number one, Pe_1 is characterized by fluid flux related to sedimentation and compaction.

$$Pe_1 = \frac{U_{f, sed} L_t}{D_m} \quad (21)$$

Similarly, Peclet number two, Pe_2 is characterized by the external fluid flux from deeper sediment.

$$Pe_2 = \frac{U_{f, ext} L_t}{D_m} \quad (22)$$

The vertical fluid flux due to sedimentation and compaction is shown as [16]:

$$U_{f, sed} = \frac{1 - \phi_o}{1 - \phi_\infty} \dot{S} \phi_\infty \quad (23)$$

The Damköhler number is a dimensionless ratio of the methanogenesis reaction to methane diffusion:

$$Da = \frac{\lambda L_t^2}{D_m} \quad (24)$$

Another dimensionless group is defined as the ratio of absolute permeability to the sedimentation rate quantifying the effects of overpressure genesis from sedimentation:

$$N_{SC} = \frac{k_0 \rho_w g}{\mu_w \dot{S}} \quad (25)$$

Large values of N_{SC} imply large sediment permeability and/or low sedimentation rate, which result in pore water pressures close to hydrostatic pressures. Conversely, smaller N_{SC} values imply low permeability and/or high sedimentation rate, thereby producing overpressure.

The ratio of characteristic compaction depth to the depth to the base of the GHSZ is defined as:

$$N'_{I\varphi} = \frac{L'_\varphi}{L_t} = \frac{\sigma_\phi / \rho_w g}{L_t} \quad (26)$$

The normalized CH₄ phase concentrations are:

$$\tilde{c}_m^l = \frac{c_m^l}{c_{m,eqb}^l} \quad \tilde{c}_m^h = \frac{c_m^h}{c_{m,eqb}^h} \quad \tilde{c}_m^g = \frac{c_m^g}{c_{m,eqb}^g} \quad (27)$$

Lithostatic stress, water, gas and capillary pressures are normalized by the hydrostatic pore water pressure at the base of the GHSZ:

$$\begin{aligned} \tilde{\sigma}_v &= \frac{\sigma_v}{\rho_w g L_t} & \tilde{P}_c &= \frac{P_c}{\rho_w g L_t} \\ \tilde{P}_w &= \frac{P_w}{\rho_w g L_t} & \tilde{P}_g &= \frac{P_g}{\rho_w g L_t} \end{aligned} \quad (28)$$

The vertical depth, lateral distance and time are scaled to the depth to the base of the GHSZ:

$$\tilde{z} = \frac{z}{L_t} \quad \tilde{x} = \frac{x}{L_t} \quad \tilde{t} = \frac{t}{L_t^2 / D_m} \quad (29)$$

All phase densities are scaled by the density of water as:

$$\tilde{\rho}_h = \frac{\rho_h}{\rho_w} \quad \tilde{\rho}_g = \frac{\rho_g}{\rho_w} \quad \tilde{\rho}_s = \frac{\rho_s}{\rho_w} \quad (30)$$

The sediment velocity is normalized by the sedimentation rate at the seafloor.

$$\tilde{v}_s = \frac{v_s}{\dot{S}} \quad (31)$$

Finally, organic carbon content and initial organic carbon content are scaled as:

$$\tilde{\alpha} = \frac{\alpha}{\alpha_0} \quad \beta = \frac{\alpha_0}{c_{m,eqb}^l} \quad (32)$$

The dimensionless mass balance equations, constitutive relationships, initial and boundary conditions are presented in the Appendix.

Numerical algorithm

The four coupled dimensionless mass balance equations (**Equations A3, A11, A14 and A17**) are solved using a fully implicit numerical scheme using the initial condition and boundary conditions discussed in the appendix. A single-point, upstream weighting was used to formulate the relative permeability terms. The primary variables are p_w , v_s , α and one of the three from the following (c_m , S_h , S_g) depending on the local thermodynamic conditions of the grid block at any given time. All the component mass balance equations are then recast in their residual form and the Newton-Raphson method is implemented to iterate on them to converge to the finite solution.

2-D model development and validation

We test, validate and benchmark our 2-D model against 1-D results [16]. The seafloor parameters used are: seafloor depth = 2700 m below sea level, seafloor temperature = 3°C, and geothermal gradient = 0.04°C/m. The primary dimensionless transport parameters defined in our model used for simulations are: $Pe_l = 0.1$, $Da = 10$, $\beta = 6$, $\eta = 6/9$, $\gamma = 9$, $N_{SC} = 10^4$ and $N'_{I\varphi} = 1.485$, unless specified otherwise. We specify critical gas saturation, S_{gr} as 100% and assume free gas to be immobile. The 2-D code was first tested with homogeneous sediment permeability (i.e., permeability changed with burial but not laterally), essentially a 1-D implementation of the 2-D model. Steady-state

hydrate and free gas saturations were simulated (**Figure 1**). The hydrate saturation with only *in situ* methane sources in a homogeneous sediment column increases to a peak saturation of $\sim 11\%$ at the base of the GHSZ with an average hydrate saturation equal to 5.7%. The 2-D profiles match the 1-D results. Due to lithologic homogeneity, the hydrate and free gas saturations are uniform laterally and this case is analogous to a simple 1-D system.

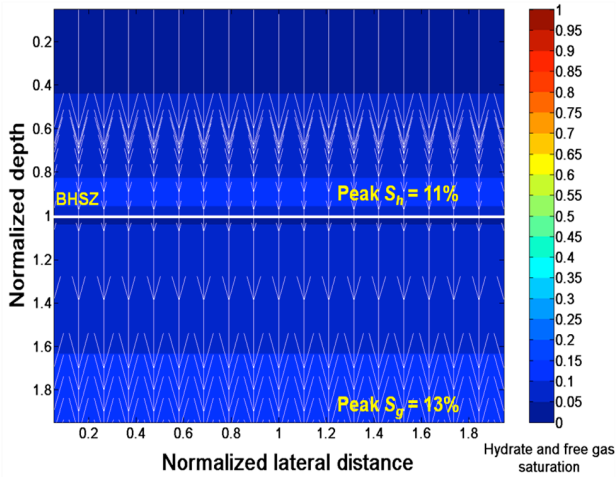


Figure 1. Steady-state hydrate and free gas saturation contours for homogeneous sediment. The white line at unit normalized depth represents the base of the GHSZ. The color bars represent hydrate and free gas saturations. The fluid flux relative to the seafloor is scaled by the maximum flux and depicted by white arrows.

There is no flow focusing or preferential accumulation of hydrate and free gas within the sediment due to absence of heterogeneity. To assess deeper methane sources, we specify a methane concentration in the pore fluid migrating upwards and simulate cases with upward fluid flux ($Pe_2 < 0$). This enables methane charged fluids to migrate upwards from deeper sources which results in higher hydrate and free gas saturations. We compute the average hydrate saturation ($\langle S_h \rangle$) within the hydrate stability zone, multiply by Pe_1 and relate this product with the net fluid flux ($Pe_1 + Pe_2$). Our results identically correlate the net fluid flux to the average hydrate saturation (**Figure 2**). Therefore, such correlations can now be used to quantify hydrate saturations using net fluid flux as the primary input.

With our validated 2-D model, we simulate heterogeneities to show how high permeability conduits localize fluid flux, and these localized fluxes result in concentrated hydrate deposits. To study heterogeneity using our 2-D model, we have considered two sources of methane: *in situ* biogenic and external deeper sources. To simulate deeper sources, we extend the model to include higher pressure at the bottom boundary to simulate higher fluid flux and methane input at depth.

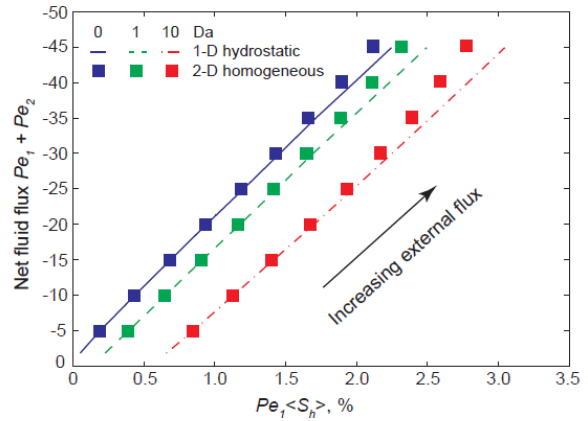


Figure 2. Average hydrate flux, $Pe_1 \langle S_h \rangle$ as a function of net fluid flux, $Pe_1 + Pe_2$ for 1-D (lines) and homogeneous 2-D sediment (squares) for a range of Da values. The assumption of negligible volume change due to methane dissolved in water in our 1-D model approximates the mass fraction of water in liquid phase, c_w^l equal to unity [16]. For our 2-D model, volume change due to methane is not assumed to be zero and thus results in a change in fluid volume when methane comes out of solution to form hydrates. Therefore, the volumetric net fluid flux, $(Pe_1 + Pe_2)$ shows a slight deviation from our 1-D results with increasing external flux.

RESULTS

Effect of vertical fracture systems

Fractures are common in geologic settings such as the Hydrate Ridge in the Cascadia Margin varying over different length scales [12,22]. Previous studies have hypothesized on the significance of fracture networks in gas hydrate systems, and we quantify their impact by implementing a vertical fracture system of higher permeability in our gas hydrate accumulation model (**Figure 3**). Vertical fracture systems are modeled since the time they are introduced ($t=0$) in the system and gas hydrate

and free gas accumulation are tracked over time. Simulations are completed with a vertical fracture system 100 times more permeable than the surrounding sediment (i.e., $N_{SC} = 10^2$ for sediment and 10^4 for the vertical fracture system).

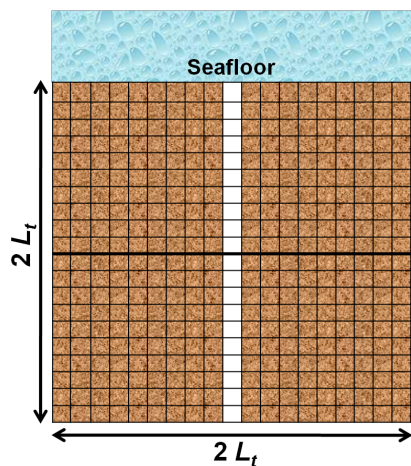


Figure 3. Schematic showing permeability map representing a vertical fracture system (white). The fracture system is 100 times more permeable than the surrounding formation. The sediment aspect ratio is 1:1.

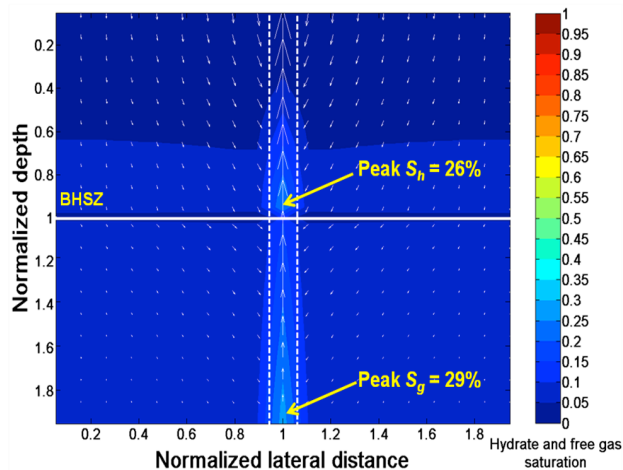


Figure 4. Steady-state gas hydrate and free gas saturation contours for isotropic system ($k_v/k_h = 1$) with biogenic *in situ* source ($Pe_2 = 0$) and a vertical fracture system. The location of the fracture is shown by a set of white, vertical dashed lines. A vector field plot shown by white arrows represents the focused fluid flow. The fluid flow within the sediment formation is in the downward direction because it is plotted relative to the seafloor. The effect of the fracture in focusing flow is clearly illustrated through enhanced

hydrate and free gas saturations within the high permeability conduit.

Simulations with a vertical fracture network, show focused fluid flow resulting in higher hydrate and free gas saturation within the high permeability fracture system compared to the surrounding lower permeability sediment. First, we consider a case with isotropic permeability. Steady-state peak hydrate saturation within the fracture system is $\sim 26\%$, while that in the surrounding sediment matrix is $\sim 10\%$ (**Figure 4**). Steady-state free gas shows peak saturation of 29% within the fracture column at the base of the domain.

We simulate a second case with a specified fluid flux from external sources at depth representing a geologic model with thermogenic methane in deeper strata. We predict higher hydrate and free gas saturation due to increased fluid flux and greater methane input into the system from deeper sources. Simulations show higher hydrate and free gas saturation within the high permeability fracture system (**Figure 5**) as compared to our case with biogenic *in-situ* methane only (**Figure 4**). Peak hydrate and free gas saturations within the fracture system are 48% and 42%, respectively.

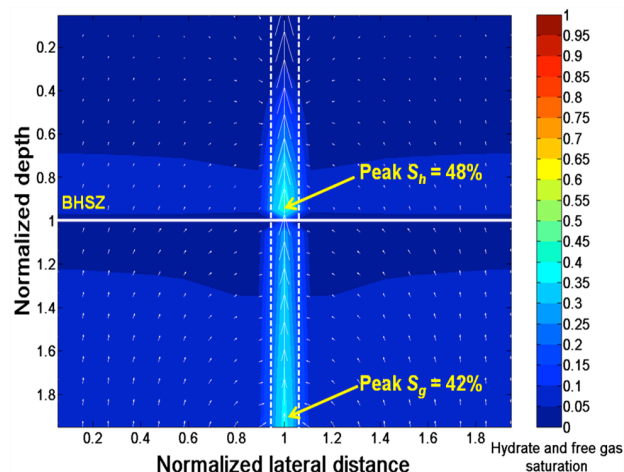


Figure 5. Steady-state gas hydrate and free gas saturation contours with a vertical fracture system, deep methane source, specified external fluid flux at the lower boundary ($Pe_2 = -2$), and all other parameters same as in **Figure 4**.

This high saturation was achieved by specifying external flux ($Pe_2 = -2$), throughout the lateral domain in the model. We show that increased fluid

flux from external sources results in higher fluid focusing which produces higher hydrate and free gas accumulations within the fracture system. As we increase the fluid flux, more dissolved methane saturated water migrates into high permeability zones which result in concentrated deposits of hydrates and free gas. Using the correlation shown above (**Figure 2**), we would expect more hydrate and free gas accumulation if higher flux was specified.

Our findings characterize the impact that high permeability vertical fractures have on gas hydrate and free gas distribution by focusing fluid flow along these fracture systems in the presence biogenic and/or thermogenic methane sources. These models quantify the effects of flow focusing.

Local flux within high permeability zones

We compute the localized, focused fluid flux and relate this local flux (Pe_{local}) to the average hydrate saturation within the high permeability conduits in the GHSZ (**Figure 6**). Our results follow the same correlation established between net fluid flux and average hydrate saturation in 1-D systems (**Figure 2**). For lower values of Da (<10), methane generated in the system is not enough for hydrate accumulation even with high local flux focused in the high permeability zones.

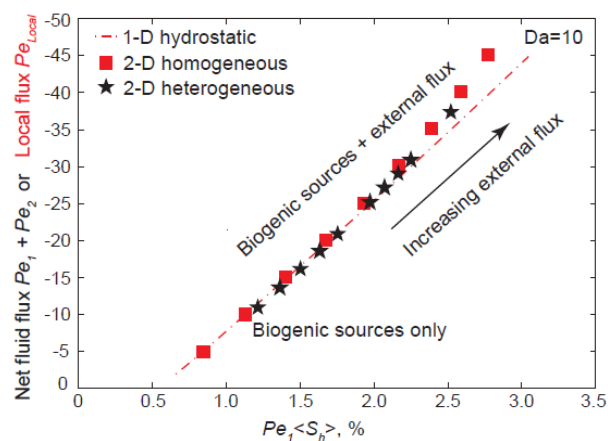


Figure 6. Steady-state average gas hydrate flux, $Pe_1 < S_h >$ and local fluid flux, Pe_{local} (black stars).

Effect of permeability anisotropy

Anisotropic cases with lower k_v/k_h ratio (order of 10^{-2}) are expected to show relatively higher hydrate saturations within the high permeability conduits as compared to isotropic cases (**Figure**

5). Simulations show peak hydrate and gas saturations are 53% and 40% respectively (**Figure 7**). Increased horizontal permeability results in more fluid flux towards the fracture system even from sediment formation farther away from the fracture column.

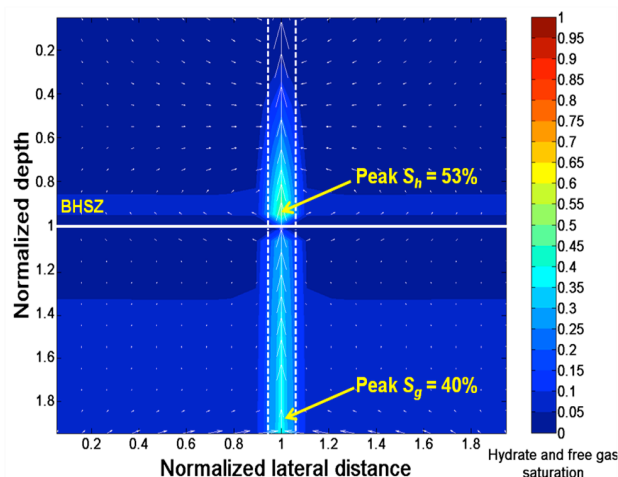


Figure 7. Steady-state gas hydrate and free gas saturation contours for an anisotropic system ($k_v/k_h=10^{-2}$) with a vertical fracture system and all other parameters same as in **Figure 5**.

Effect of free gas migration into the GHSZ

Focusing of liquid (water) enhances hydrate and free gas saturations within the high permeability zones. However, free gas can also migrate vertically and laterally if the critical gas saturation is exceeded. To simulate such migration, critical gas saturation (S_{gr}) is set to 5% and free gas exceeding this critical value is free to migrate. Free gas migrates upwards due to buoyancy and gets sealed by the low permeability hydrate layer at the base of the GHSZ. Hydrate formation at the base of the GHSZ causes an increase in the capillary entry pressure and creates a hindrance for free gas to enter the GHSZ from below. This results in accumulation of free gas beneath the GHSZ into a connected gas column.

Simulations show free gas accumulation below the base of the GHSZ (**Figure 8**). A long gas column is formed before the gas pressure exceeds the capillary entry pressure and gas migrates into the GHSZ. Free gas converts to hydrate immediately at the base of the GHSZ giving rise to a spike in hydrate saturation. We assume constant salinity therefore phase equilibrium is unaffected even

when free gas migrates into the GHSZ. The high hydrate saturation in the fracture zone causes a permeability reduction which in turn creates lateral fluid migration beneath the GHSZ. High hydrate saturation also restricts further free gas invasion into the GHSZ. Free gas then migrates laterally from the high permeability fracture system to the neighboring sediment below the base of the GHSZ. Peak hydrate and free gas saturation reaches 75% and 62% right above and below the base of the GHSZ within the fracture system. At this enhanced saturation, free gas is mobile and migrates laterally, causing sediment near the fracture to also have relatively higher saturations.

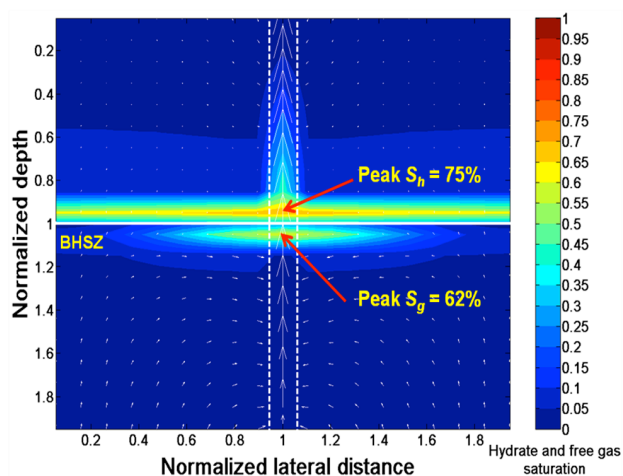


Figure 8. Steady-state gas hydrate and free gas saturation contours for an isotropic system with a vertical fracture system, mobile gas ($S_{gr} = 5\%$) and all other parameters same as in **Figure 5**.

The length of a connected gas column has been shown to be dependent on the dimensionless group N_{SC} [23]. Lower values of N_{SC} (lower permeability and/or higher sedimentation rate) result in development of higher overpressure in the system, which further results in thicker gas columns and increased gas pressure at the base of the GHSZ close to the lithostatic stress. Fractures tend to open up at this point [24]. This fracturing process is not modeled in any of our simulations, and our simulations are terminated as soon as gas pressure equals total vertical stress.

Effect of high permeability sand layers

To look at lithologic heterogeneity, we incorporate dipping sand beds bounded by low permeability shale. To model a sand layer, we include a high

permeability sand layer at a given dip angle ($\sim 3^\circ$) within the sediment (**Figure 9**) and bury it through geologic time. The downward movement of this sand layer and the corresponding transient hydrate and free gas evolution are recorded. The sand layer is assigned an absolute permeability 100 times greater than the surrounding shale. Sediment compacts with burial ($N_{SC} = 10^2$ for shale and 10^4 for sand layers). The seafloor and transport parameters are same as in the simulations with vertical fracture network except $Da = 1$. During burial, absolute permeability of any grid block can be computed by interpolation and therefore, interface between zones of different permeabilities are recorded over time. The interface position is used to compute the horizontal and vertical permeabilities and track the location of the sediment over time.

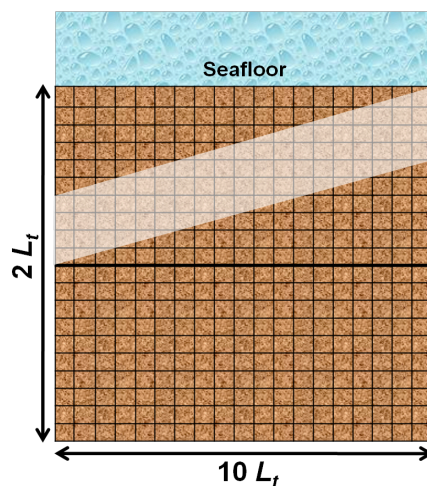


Figure 9. Schematic showing initial permeability map representing high permeability sand layer (white) deposited between two low permeability sediment layers. The sand layer is 100 times more permeable than the surrounding formation. A 5:1 vertical exaggeration is used to plot the sediment.

Systems with dipping sand layers show localized, enhanced concentrations of hydrate and free gas within the high permeability sand layers (**Figure 10**). Free gas is focused within the sand layer. Steady-state peak hydrate saturation within the sand layer is about 59%, significantly higher than the 43% peak hydrate saturation in the low permeability sediment within the GHSZ. Peak free gas saturation is 38% within the sand layer just below the GHSZ, and similar to fracture network case (**Figure 8**), free gas migrates laterally into the

low permeability sediment around the sand layer. Thus, presence of higher permeability sand layer leads to relatively higher fluid focusing and hydrate saturation within the GHSZ. Our results elucidate that lithology plays a significant role in accumulating gas hydrate and free gas in heterogeneous sediment in most natural systems.

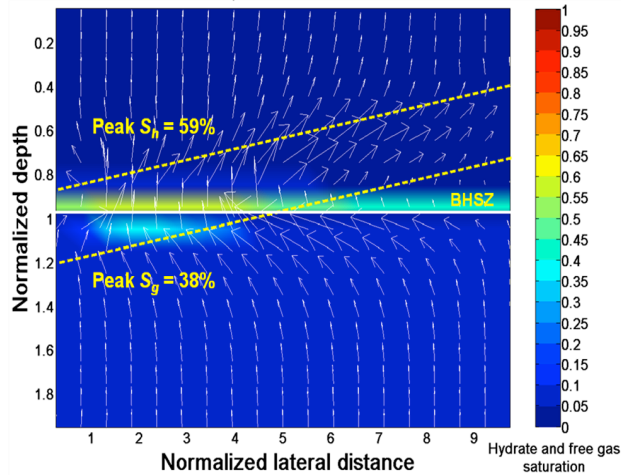


Figure 10. Steady-state hydrate and free gas saturation contours for a system with high permeability dipping sand bed between two anisotropic ($k_v/k_h = 10^{-2}$) shale beds. The position of the sand layer is depicted by the set of yellow dashed lines. Vertical exaggeration of 5:1 is used and the physical domain for normalized depth and lateral distance are $[0, 2]$ and $[0, 10]$, respectively.

CONCLUSIONS

A generalized 2-D model was developed to simulate gas hydrate and free gas accumulation in heterogeneous marine sediment. Our model allows incorporation of lithologic heterogeneity and lateral fluid flow in the system. Focused fluid flow through a vertical fracture network or high permeability sand layers increase local hydrate accumulation and saturation. Currently, relatively simple systems with fracture systems and/or dipping sand layers are simulated, whereas realistic geologic settings are characterized by much more heterogeneous stratigraphy in terms of vertical fracture networks, multiple sand layers embedded within shale layers and fracture connectivity of sand layers with vertical fracture systems. These preliminary results, however, serve as a starting point and demonstrate that heterogeneity in natural gas hydrate systems is important for controlling hydrate and free gas

saturations, and that these systems can be modeled. Simulations with specified fluid flux and methane input from deeper sources, allows comparison of local methanogenesis and deeper methane sources on flow pathways and hydrate/free gas accumulation. We show that increased fluid flux from deeper external sources results in increased concentrations of hydrate and free gas. Permeability anisotropy, with a lower ratio of vertical to horizontal permeability show enhanced hydrate concentrations within the high permeability conduits because anisotropy focuses more methane-charged fluid into these conduits. In our 2-D work, we show that the localized, focused, advective flux relative to diffusion (Pe_{local}) determines the magnitude of hydrate and free gas saturation. We relate average local Peclet numbers and average hydrate flux ($Pe_l < S_h >$) within high permeability conduits, which compare favorably with our previous 1-D correlation.

ACKNOWLEDGEMENTS

We acknowledge financial support from the Shell Center for Sustainability, and the Department of Energy (DE-FC26-06NT42960).

REFERENCES

- [1] Sloan EDJ, Koh CA. *Clathrate hydrates of natural gases*. CRC Press 2007.
- [2] Dickens GR. *The potential volume of oceanic methane hydrates with variable external conditions*. *Organic Geochemistry* 2001; 32:1179-1193.
- [3] Archer D. *Methane hydrate stability and anthropogenic climate change*. *Biogeosciences* 2007; 4:521-544.
- [4] Collett TS. *Energy resource potential of natural gas hydrates*. *American Association of Petroleum Geologists Bulletin* 2002; 86:1971-1992.
- [5] Walsh MR, Hancock SH, Wilson SJ, Patil SL, Moridis GJ, Boswell R, Collett TS, Koh CA, Sloan EDJ. *Preliminary report on the commercial viability of gas production from natural gas hydrates*. *Energy Economics* 2009; 31:815-823.
- [6] Briaud JL, Chaouch A. *Hydrate melting in soil around hot conductor*. *Journal of Geotechnical and Geoenvironmental Engineering* 1997; 123:645-653.
- [7] Kwon TH, Song KI, Cho GC. *Destabilization of Marine Gas Hydrate-Bearing Sediments Induced by a Hot Wellbore: A Numerical Approach*. *Energy and Fuels* 2010; 24:5493-5507.

[8] Dickens GR. *Rethinking the global carbon cycle with a large, dynamic and microbially mediated gas hydrate capacitor*. Earth and Planetary Science Letters 2003; 213:169-183.

[9] Archer D, Buffett BA, Brovkin V. *Ocean methane hydrates as a slow tipping point in the global carbon cycle*. Proceedings of the National Academy of Sciences of the United States of America 2009; 106(49):20596-20601.

[10] Cook AE, Goldberg D, Kleinberg RL. *Fracture-controlled gas hydrate systems in the northern Gulf of Mexico*. Marine and Petroleum Geology 2008; 25(9):932-941.

[11] Malinverno A, Kastner M, Torres ME, Wortmann UG. *Gas hydrate occurrence from pore water chlorinity and downhole logs in a transect across the northern Cascadia margin (Integrated Ocean Drilling Program Expedition 311)*. Journal of Geophysical Research 2008; 113(B08):103, doi:10.1029/2008JB005702.

[12] Weinberger JL, Brown KM. *Fracture networks and hydrate distribution at Hydrate Ridge, Oregon*. Earth and Planetary Science Letters 2006; 245(1):123-136.

[13] Rempel AW, Buffett BA. *Formation and accumulation of gas hydrate in porous media*. Journal of Geophysical Research 1997; 102:10151-10164.

[14] Xu W, Ruppel C. *Predicting the occurrence, distribution, and evolution of methane gas hydrate in porous marine sediments*. Journal of Geophysical Research 1999; 104:5081-5096.

[15] Davie MK, Buffett BA. *A numerical model for the formation of gas hydrate below the seafloor*. Journal of Geophysical Research 2001; 106:497-514.

[16] Bhatnagar G, Chapman WG, Dickens GR, Dugan B, Hirasaki GJ. *Generalization of gas hydrate distribution and saturation in marine sediments by scaling of thermodynamic and transport processes*. American Journal of Science 2007; 307:861-900.

[17] Bhatnagar G. *Accumulation of gas hydrates in marine sediments*. Ph.D. dissertation, Rice University 2008; p. 192-236.

[18] Bear J. *Dynamic of fluids in porous media*. New York: Dover Publications Inc., 1988.

[19] Smith JE. *The dynamics of shale compaction and evolution of pore-fluid pressures*. Mathematical Geology 1971; 3:239-263.

[20] Kleinberg RL, Flaum C, Griffin DD, Brewer PG, Malby GE, Peltzer ET, Yesinowski JP. *Deep sea NMR: Methane hydrate growth habitat in*

porous media and its relationship to hydraulic permeability, deposit accumulation, and submarine slope stability. Journal of Geophysical Research 2003; 108(B10):2508, doi:10.1029/2003JB002389.

[21] Rubey WW, Hubbert MK. *Role of fluid pressure in mechanics of over-thrust faulting; ii. Overthrust belt in geosynclinal area of western Wyoming in light of fluid pressure hypothesis*. Geological Society of America Bulletin 1959; 70:167-206.

[22] Tréhu AM, Long PE, Torres ME, Bohrmann G, Rack FR, Collett TS, et al. *Three-dimensional distribution of gas hydrate beneath southern Hydrate Ridge: Constraints from ODP Leg 204*. Earth and Planetary Science Letters 2004; 222: 845-862.

[23] Bhatnagar G, Chapman WG, Dickens GR, Dugan B, Hirasaki GJ. *Effect of Overpressure on Gas Hydrate Distribution*. Proceedings of the 6th International Conference on Gas Hydrates (ICGH), Vancouver, Canada, 2008.

[24] Daigle H, Dugan B. *Origin and evolution of fracture-hosted methane hydrate deposits*. Journal of Geophysical Research 2010; 115(B11):103, doi:10.1029/2010JB007492.

APPENDIX

A1. Initial porosity profile

Reduced porosity is related to the dimensionless lithostatic stress and dimensionless pore pressure:

$$\tilde{\phi} = \eta \exp \left[-\frac{\tilde{\sigma}_v - \tilde{p}_w}{N'_{\phi}} \right] \quad (\text{A1})$$

At hydrostatic pressure, the porosity profile can be calculated as an analytical expression to serve as an initial condition:

$$\tilde{\phi} = \frac{\eta}{\eta + (1 - \eta) \exp \left[\frac{\gamma \tilde{z} (\tilde{\rho}_s - 1)}{N'_{\phi} (1 + \gamma)} \right]} \quad (\text{A2})$$

A2. Dimensionless mass balances

The four mass balance equations (**Equations 1-4**) are normalized using the scaling scheme discussed in the main text and recast in their dimensionless form with their corresponding initial condition (I.C.) and boundary conditions (B.C.).

Water mass balance:

$$\begin{aligned} & \frac{\partial}{\partial \tilde{t}} \left[\left(\frac{1+\gamma\tilde{\phi}}{\gamma} \right) (S_w \tilde{c}_w^l + S_h \tilde{c}_w^h \tilde{\rho}_h) \right] + Pe_1 \left(\frac{1+\gamma}{1-\eta} \right) \\ & \left[\begin{aligned} & \frac{\partial}{\partial \tilde{z}} \left[\left(\frac{1+\gamma\tilde{\phi}}{\gamma} \right) (S_w \tilde{c}_w^l + S_h \tilde{c}_w^h \tilde{\rho}_h) \tilde{v}_s \right. \\ & \left. - N_{sc} k_{rw} \left(\frac{1+\gamma}{\gamma} \right) \left(\frac{1+\gamma\tilde{\phi}}{1+\gamma\eta} \right)^8 \left(\frac{\partial \tilde{p}_w}{\partial \tilde{z}} - 1 \right) \tilde{c}_w^l \right] \\ & + \frac{\partial}{\partial \tilde{x}} \left[-N_{sc} \left(\frac{1+\gamma}{\gamma} \right) \left(\frac{1+\gamma\tilde{\phi}}{1+\gamma\eta} \right)^8 k_{rw} \left(\frac{\partial \tilde{p}_w}{\partial \tilde{x}} \right) \tilde{c}_w^l \right] \right] \\ & = 0 \end{aligned} \quad (A3) \end{aligned}$$

The initial condition (I.C.) is assumed to be hydrostatic. The boundary condition (B.C.) at the seafloor is assumed hydrostatic, and the left and right extremes of the domain are considered as no-flow boundaries. The initial condition and boundary conditions are expressed as follows:

$$\text{I.C.: } \tilde{p}_w(\tilde{z}, \tilde{x}, 0) = \frac{\rho_w g L_o + \rho_w g \tilde{z}}{\rho_w g L_t} = \frac{L_o}{L_t} + \tilde{z} \quad (A4)$$

$$\text{B.C.(1): } \tilde{p}_w(0, \tilde{x}, \tilde{t}) = \frac{L_o}{L_t} \quad (A5)$$

$$\text{B.C.(2): } \frac{\partial \tilde{p}_w}{\partial \tilde{x}}(\tilde{z}, 0, \tilde{t}) = \frac{\partial \tilde{p}_w}{\partial \tilde{x}}(\tilde{z}, L_x, \tilde{t}) = 0 \quad (A6)$$

The pore pressures in our 2-D model are no longer hydrostatic, so the pressure gradient at the lowermost boundary cannot be modeled as a hydrostatic pressure gradient $\frac{\partial \tilde{p}_w}{\partial \tilde{z}}(L_z, \tilde{x}, \tilde{t}) = 1$.

The bottommost boundary has been modeled by specifying the fluid flux and thereby specifying a constant non-hydrostatic pressure gradient. The specified fluid flux is equal to $U_{f, sed} + U_{f, ext}$ (for biogenic sources only, $U_{f, ext} = 0$). We rewrite our Darcy water flux (**Equation 5**) for the lowermost boundary as follows:

$$\begin{aligned} v_w S_w \phi &= v_s S_w \phi - \frac{k k_{rw}}{\mu_w} \cdot (\nabla p_w - \rho_w g \nabla z) \\ &= U_{f, sed} + U_{f, ext} \end{aligned} \quad (A7)$$

On normalizing, we get:

$$\begin{aligned} \tilde{v}_w S_w \frac{1+\gamma\tilde{\phi}}{\gamma} &= \tilde{v}_s S_w \frac{1+\gamma\tilde{\phi}}{\gamma} - k_{rw} \left(\frac{1+\gamma}{\gamma} \right) \left(\frac{k_o \rho_w g}{\tilde{S} \mu_w} \right) \\ \left(\frac{k}{k_o} \right) \cdot (\nabla \tilde{p}_w - \nabla \tilde{z}) &= \frac{1+\gamma}{\gamma} \frac{[U_{f, sed} + U_{f, ext}]}{\tilde{S}} \end{aligned} \quad (A8)$$

Substituting **Equations 23** and **25**, normalizing the term on the right and rearranging, we get:

$$\begin{aligned} & -N_{sc} \left(\frac{1+\gamma}{\gamma} \right) \left(\frac{k}{k_o} \right) k_{rw} \cdot (\nabla \tilde{p}_w - \nabla \tilde{z}) \\ &= \frac{[Pe_1 + Pe_2]}{Pe_1 \gamma / 1 - \eta} - \left(\frac{1+\gamma\tilde{\phi}}{\gamma} \right) S_w \tilde{v}_s \end{aligned} \quad (A9)$$

The non-hydrostatic pressure gradient at the bottom boundary is expressed using **Equation A9**:

$$\frac{\partial \tilde{p}_w}{\partial \tilde{z}}(L_z, \tilde{x}, \tilde{t}) = 1 - \frac{\frac{[Pe_1 + Pe_2]}{Pe_1 \gamma / 1 - \eta} - \left(\frac{1+\gamma\tilde{\phi}}{\gamma} \right) S_w \tilde{v}_s}{N_{sc} \left(\frac{1+\gamma}{\gamma} \right) \left(\frac{1+\gamma\tilde{\phi}}{1+\gamma\eta} \right)^8 k_{rw}(L_z)} \quad (A10)$$

Notably, the relative permeability of water at this boundary is unity. Thus, a non-hydrostatic boundary condition at the lowermost boundary (**Equation A10**) is derived by specifying a finite fluid flux at the boundary. Infinite N_{SC} represents infinite permeability, which implies hydrostatic conditions. For $N_{SC} = \infty$, **Equation A10** reduces the pressure gradient to unity which corresponds to a hydrostatic pressure gradient at the lowermost boundary of our simulation domain.

Sediment mass balance:

$$\frac{\partial}{\partial \tilde{t}} (1 - \tilde{\phi}) + Pe_1 \left(\frac{1+\gamma}{1-\eta} \right) \frac{\partial}{\partial \tilde{z}} [(1 - \tilde{\phi}) \tilde{v}_s] = 0 \quad (A11)$$

The initial sediment velocity profile is evaluated assuming hydrostatic pressure, whereas the boundary condition for velocity of sediment at the seafloor is the normalized sedimentation rate and equal to unity.

$$\text{I.C.:} \quad \tilde{v}_s(\tilde{z}, \tilde{x}, 0) = \left(\frac{1-\eta}{1-\tilde{\phi}} \right) \quad (\text{A12})$$

$$\text{B.C.:} \quad \tilde{v}_s(0, \tilde{x}, \tilde{t}) = 1 \quad (\text{A13})$$

Organic mass balance:

$$\begin{aligned} & \frac{\partial}{\partial \tilde{t}} \left[(1-\tilde{\phi})\tilde{\alpha} \right] + Pe_1 \left(\frac{1+\gamma}{1-\eta} \right) \frac{\partial}{\partial \tilde{z}} \left[(1-\tilde{\phi})\tilde{v}_s\tilde{\alpha} \right] \\ & = -Da(1-\tilde{\phi})\tilde{\alpha} \end{aligned} \quad (\text{A14})$$

Initially, there is no organic carbon present within the sediment, whereas the boundary condition of organic concentration at the seafloor is normalized to unity.

$$\text{I.C.:} \quad \tilde{\alpha}(\tilde{z}, \tilde{x}, 0) = 0 \quad (\text{A15})$$

$$\text{B.C.:} \quad \tilde{\alpha}(0, \tilde{x}, \tilde{t}) = 1 \quad (\text{A16})$$

Methane mass balance:

$$\begin{aligned} & \frac{\partial}{\partial \tilde{t}} \left[\left(\frac{1+\gamma\tilde{\phi}}{\gamma} \right) (S_w\tilde{c}_m^l + S_h\tilde{c}_m^h\tilde{\rho}_h + S_g\tilde{c}_m^g\tilde{\rho}_g) \right] + Pe_1 \left(\frac{1+\gamma}{1-\eta} \right) \\ & \left[\begin{array}{l} \frac{\partial}{\partial \tilde{z}} \left[\left(\frac{1+\gamma\tilde{\phi}}{\gamma} \right) (S_w\tilde{c}_m^l + S_h\tilde{c}_m^h\tilde{\rho}_h + S_g\tilde{c}_m^g\tilde{\rho}_g) \tilde{v}_s \right] \\ -N_{sc}k_{rw} \left(\frac{1+\gamma}{\gamma} \right) \left(\frac{1+\gamma\tilde{\phi}}{1+\gamma\eta} \right)^8 \left(\frac{\partial \tilde{p}_w}{\partial \tilde{z}} - 1 \right) \tilde{c}_m^l \\ \frac{\partial}{\partial \tilde{z}} \left[-N_{sc}k_{rg}\tilde{\rho}_g \frac{\mu_w}{\mu_g} \left(\frac{1+\gamma}{\gamma} \right) \left(\frac{1+\gamma\tilde{\phi}}{1+\gamma\eta} \right)^8 \left(\frac{\partial \tilde{p}_g}{\partial \tilde{z}} - \tilde{\rho}_g \right) \tilde{c}_m^g \right] \\ \frac{\partial}{\partial \tilde{x}} \left[-N_{sc}k_{rw} \left(\frac{1+\gamma}{\gamma} \right) \left(\frac{1+\gamma\tilde{\phi}}{1+\gamma\eta} \right)^8 \left(\frac{\partial \tilde{p}_w}{\partial \tilde{x}} \right) \tilde{c}_m^l \right] \\ -N_{sc} \left(\frac{1+\gamma}{\gamma} \right) \left(\frac{1+\gamma\tilde{\phi}}{1+\gamma\eta} \right)^8 k_{rg} \left(\frac{\partial \tilde{p}_g}{\partial \tilde{x}} \right) \left(\frac{\mu_w}{\mu_g} \right) \tilde{\rho}_g \tilde{c}_m^g \end{array} \right] \\ & = \frac{\partial}{\partial \tilde{z}} \left[\left(\frac{1+\gamma\tilde{\phi}}{\gamma} \right) S_w \frac{\partial \tilde{c}_m^l}{\partial \tilde{z}} \right] + \frac{\partial}{\partial \tilde{x}} \left[\left(\frac{1+\gamma\tilde{\phi}}{\gamma} \right) S_w \frac{\partial \tilde{c}_m^l}{\partial \tilde{x}} \right] \\ & + \frac{M_{CH_4}}{M_{org}} \tilde{\rho}_s Da(1-\tilde{\phi})\tilde{\alpha}\beta \end{aligned} \quad (\text{A17})$$

Initially, there is no methane in the system. At the seafloor, methane concentration is equal to zero;

methane flux is set to zero at the right and left extremes of the domain; the bottom boundary has a choice of boundary condition, depending on the methane source. The methane concentration gradient is equal to zero for a system with biogenic sources only (**Equation A21**), whereas the methane concentration is set to be a constant value for deeper methane sources (**Equation A22**).

$$\text{I.C.:} \quad \tilde{c}_m(\tilde{z}, \tilde{x}, 0) = 0 \quad (\text{A18})$$

$$\text{B.C.(1):} \quad \tilde{c}_m(0, \tilde{x}, \tilde{t}) = 0, \quad (\text{A19})$$

$$\text{B.C.(2):} \quad \frac{\partial \tilde{c}_m^l}{\partial \tilde{x}}(\tilde{z}, 0, \tilde{t}) = \frac{\partial \tilde{c}_m^l}{\partial \tilde{x}}(\tilde{z}, L_x, \tilde{t}) = 0 \quad (\text{A20})$$

$$\text{B.C.(3):} \quad \frac{\partial \tilde{c}_m^l}{\partial \tilde{z}}(L_z, \tilde{x}, \tilde{t}) = 0 \quad (\text{A21})$$

$$\text{B.C.(4):} \quad \tilde{c}_m^l(L_z, \tilde{x}, \tilde{t}) = \tilde{c}_{m,ext}^l \quad (\text{A22})$$